

Tuning the Electronic and Molecular Structures of Catalytic Active Sites with Oxide Support Nanoligands

*I.E. Wachs**, *A. Burrows**, *C. Kiely** and *E.I. Ross**

**Operando Molecular Spectroscopy and Catalysis Lab., Dept. of Chemical Engineering,*

**Nanotechnology Characterization Center, Dept. of Materials Science & Engineering.,
Lehigh University, Bethlehem, PA 18015 USA*

Introduction

Supported metal and metal oxide catalytic materials represent the catalyst workhorses of the environmental, energy and petrochemical industries [1-3]. The catalytic performance of supported metal and metal oxide catalytic active sites is known to depend on their synthesis method, dispersion, morphology, support interaction, as well as presence of secondary additives (promoters and poisons). It has been well documented that the nature of the active metal or metal oxide component-support interaction has a pronounced effect on the catalytic performance, and is many times the most significant effect among the different catalyst variables. This catalytic enhancement is proposed to occur for many systems through charge transfer between the metal or metal oxide active component and the underlying oxide support ligand [4-11]. Such a charge transfer can modify the electron density of nano-sized metal and metal oxide catalytic active sites with a consequent modification of the catalytic performance.

The electron density of nano-sized metal oxide clusters is known to be dependent on the metal oxide domain size, with the local electron density increasing for smaller dimensions and the electrons becoming more delocalized for larger dimensions [12]. Consequently, nano-oxide support substrates exhibit variable electron density that can be shared with the supported active metal or metal oxide components that contain the catalytic active sites [13]. This suggests that higher local electron density, less delocalized electrons, of such nano-supports will enhance the catalytic performance of supported metallic catalysts and acidic supported metal oxide catalysts that don't undergo reduction [4].

Metal oxide nano-domains were synthesized by impregnating a relatively inert and high surface area amorphous SiO_2 support (15-30 nm) with Ti-isopropoxide dissolved in isopropanol to form the supported nano-titania phases on the SiO_2 matrix. The presence of the SiO_2 matrix is *critical* in preventing agglomeration of the titania to form large domains. These catalysts were then used to obtain a series of model multilayered $\text{WO}_3/\text{TiO}_2/\text{SiO}_2$ and $\text{V}_2\text{O}_5/\text{TiO}_2/\text{SiO}_2$ samples to explore the fundamental aspects for tuning the electronic and molecular structures of supported catalytic active sites for enhanced catalytic performance of acidic surface WO_x and redox VO_x species.

Experimental

Catalyst Preparation

A series of supported $\text{TiO}_2/\text{SiO}_2$, acidic supported $\text{WO}_3/\text{TiO}_2/\text{SiO}_2$, and redox $\text{V}_2\text{O}_5/\text{TiO}_2/\text{SiO}_2$ catalysts were synthesized by incipient wetness impregnation. The SiO_2 support used for this study was Cab-O-Sil EH-5 (BET=332 m^2/g). The supported $\text{TiO}_2/\text{SiO}_2$

catalysts were prepared by the incipient wetness impregnation of 2-propanol solutions of titanium isopropoxide ($\text{Ti}(\text{O-Pr}^i)_4$, Alfa-Aesar, 99.999% purity). The preparation was performed inside a glovebox with continuously flowing N_2 . The SiO_2 support was initially dried at 120°C to remove the physisorbed water before impregnation. After impregnation at room temperature, the samples were kept inside the glovebox with flowing N_2 overnight. The samples were subsequently dried at 120°C in flowing N_2 for 1 h and calcined at 500°C in flowing air for 4 h. A two-step preparation procedure was employed to prepare samples with loadings higher than 8 wt % TiO_2 . The second impregnation followed the same procedure described above by using 8% $\text{TiO}_2/\text{SiO}_2$ as the starting material to prepare 10%, 12%, and 15% $\text{TiO}_2/\text{SiO}_2$ catalysts. Multiple impregnation steps were used to prepare samples with loadings higher than 15% TiO_2 [14]. A series of 5% WO_3 /x% $\text{TiO}_2/\text{SiO}_2$ catalysts were prepared by the incipient wetness impregnation of aqueous ammonium metatungstate solutions onto the various supported $\text{TiO}_2/\text{SiO}_2$ samples. The resulting samples were then dried in flowing air at 120°C for 1 h, 300°C for 1 h, and finally calcined at 500°C for 2 h. The multilayered 5% V_2O_5 /x% $\text{TiO}_2/\text{SiO}_2$ catalysts were prepared by the incipient wetness impregnation of 2-propanol solutions of vanadium isopropoxide ($\text{VO}(\text{O-Pr}^i)_3$, Alfa-Aesar 97 % purity) onto the various weight percents of the $\text{TiO}_2/\text{SiO}_2$ samples. The preparation was performed within a glovebox with continuously flowing N_2 and the supports were initially dried at 120°C to remove physisorbed water before impregnation, and then kept within the glovebox overnight after impregnation. The resulting samples were then dried in flowing N_2 at 120°C for 1 h and 300°C for 1 h. The $\text{V}_2\text{O}_5/\text{TiO}_2/\text{SiO}_2$ samples were calcined flowing air at 300°C for 1 h and 500°C for 2 h.

Raman Spectroscopy

The Raman spectra were obtained using a new state-of-the-art UV-VIS Raman spectrometer (Jobin Yvon LabRam HR) equipped with a notch filter to reject the Rayleigh scattering, a single monochromator stage, and a CCD detector cooled to 140 K. The excitation source employed was 532 nm from an Ar^+ laser (Spectra Physics, Model 164) and the scattered photons were directed and focused onto the monochromator. The Raman spectra of the dehydrated samples, in loose powder form, were recorded at room temperature after heating the samples in flowing O_2/He at 500°C for 1 h in a stationary cell (Linkam T1500).

UV-Vis Diffuse Reflectance Spectroscopy (DRS)

DRS spectra in the range of 200-800 nm were measured on a Varian Cary 5 UV-vis-NIR spectrophotometer. The spectra were recorded against a magnesium oxide reflectance standard as the baseline. The processing of the spectra consists of the calculation of the Kubelka-Munk function ($F(R_{\infty})$) from the absorbance. The edge energy, E_g , for the allowed transitions was determined by finding the intercept of the straight line in the low-energy rise of the plot of $[F(R_{\infty}) \times hv]^2$ against hv , where hv is the incident photon energy [15]. The spectra of the dehydrated samples were obtained after the samples were calcined at 400°C in flowing O_2/He for 1 h and cooled to room temperature.

TEM

TEM images were obtained using a JEOL 4000EX microscope, having an accelerating voltage of 400 keV, a point-to-point resolution of 1.9 Angstroms and an information limit of 1.4 Angstroms. Fourier transform (FT) analyses of the lattices fringe images obtained were carried out using Digital Micrograph.

CH₃OH-Temperature Programmed Surface Reaction (TPSR) Spectroscopy

Methanol-TPSR was performed on an Altamira Instruments temperature programmed system (AMI-200) equipped with an online quadrupole mass spectrometer (Dycor Dymaxion DME200MS). Approximately 100 mg of sample was loaded into a U-shaped quartz tube and initially calcined at 350 °C in the presence of ultra zero grade O₂/He at 30 ml/min for ~1 h to remove any possible adsorbed impurities and moisture. The pretreated samples were then cooled in flowing air to 110°C, and then further cooled to 100 °C in an ultra high purity He flow. After continuously flushing with flowing He for ~1 hour at 100°C to remove any physically adsorbed oxygen and background gases, a CH₃OH/He gas mixture feed (30 ml/min) containing 2000 ppm methanol was introduced for chemisorption and maintained for 30 minutes. Earlier work showed that the adsorption temperature of 100°C minimizes the formation of physically adsorbed methanol on the samples since physically adsorbed CH₃OH desorbs below 100°C [16, 17]. After methanol adsorption, the samples were purged at 100 °C with a He flow for an additional 1 h to remove any residual physically adsorbed methanol. The CH₃OH-TPSR experiments were then performed in an UHP He flow with a heating rate of 10°C/min. The exit gases were monitored with the online mass spectrometer. The *m/e* values employed to detect the different desorption products are as follows: *m/e*=31 for CH₃OH, *m/e*=30 for H₂CO, *m/e*=45 for CH₃OCH₃ (DME), *m/e*=76 for (CH₃O)₂CH₂ (DMM), *m/e*=44 for CO₂, *m/e*=28 for CO and *m/e*=18 for H₂O. The CH₃OH molecule can discriminate between types of surface sites [18, 19]: Surface acidic sites yield CH₃OCH₃, dimethyl ether (DME), surface basic sites primarily produce CO/CO₂ and some H₂CO, and surface redox sites exclusively yield H₂CO, formaldehyde. Furthermore, dual surface acidic-redox sites tend to form (CH₃O)₂CH₂, dimethoxy methane (DMM), and dual surface basic-redox sites tend to result in formation of CH₃OOCH, methyl formate (MF).

Results & Discussion

Supported TiO₂/SiO₂. The electronic and molecular structures of the series of supported TiO₂/SiO₂ samples were examined with *in situ* UV-Vis and *in situ* Raman spectroscopy, respectively. Raman and UV-vis spectroscopy revealed that the 1% TiO₂/SiO₂ sample consists of isolated surface TiO₄ species and that the 12% TiO₂/SiO₂ sample consists of a two-dimensional monolayer of polymeric surface TiO₅ species (see Table 1). *In situ* XANES measurements confirmed the coordination of the surface TiO_x species. Additional structural information was provided by transmission electron microscopy (TEM). Bright field images and selected area electron diffraction patterns showed no obvious signs of TiO₂ crystallites (see Figure 2a) and EDS elemental analysis confirmed the presence of surface TiO_x on the amorphous SiO₂ particles. Raman revealed that above monolayer surface coverage (>12% TiO₂) crystalline TiO₂(anatase), nanoparticles (NPs) were present in the TiO₂/SiO₂ samples (see Figure 1). The TiO₂(A) NPs consumed the surface TiO_x layer due to the greater affinity of the surface TiO_x species for the TiO₂(A) nanocrystals over the relatively inert SiO₂ support surface. However, 20% TiO₂/SiO₂ showed intermediate behavior, possessing a mixture of surface TiO_x and 2-4 nm TiO₂(A) nanocrystallites. The 40 wt%

TiO₂/SiO₂ sample (see Figure 2b), however, was found to exclusively contain 3-6 nm TiO₂ crystallites (observed as darker patches on the SiO₂ support). Selected area diffraction patterns confirmed that the TiO₂ NPs possessed the anatase structure.

Table 1: TiO₂ domain size for the supported TiO₂/SiO₂ catalysts

Sample	Structure	Domain Size (nm)
1 % TiO ₂ /SiO ₂	Isolated surface TiO ₄ species	~0.4 nm
5 % TiO ₂ /SiO ₂	Isolated surface TiO ₄ & polymeric surface TiO ₅ species	~0.7-0.8 nm
12 % TiO ₂ /SiO ₂	Polymeric surface TiO ₅ species	~1 nm**
20 % TiO ₂ /SiO ₂	Polymeric surface TiO ₅ species & TiO ₂ (A)	2-4 nm
30 % TiO ₂ /SiO ₂	TiO ₂ (A)	3-5 nm
40 % TiO ₂ /SiO ₂	TiO ₂ (A)	3-6 nm

* Estimated for isolated TiO₄ unit

** Estimated for surface TiO₅ polymer

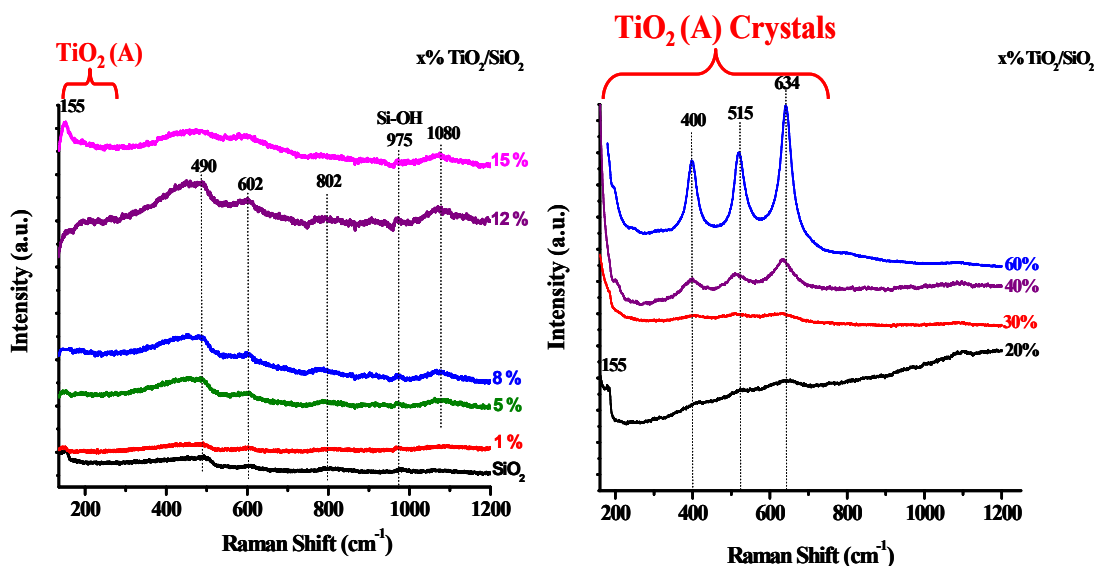


Figure 1: Raman spectrum of supported TiO₂/SiO₂ samples [100-1200 cm⁻¹ region]

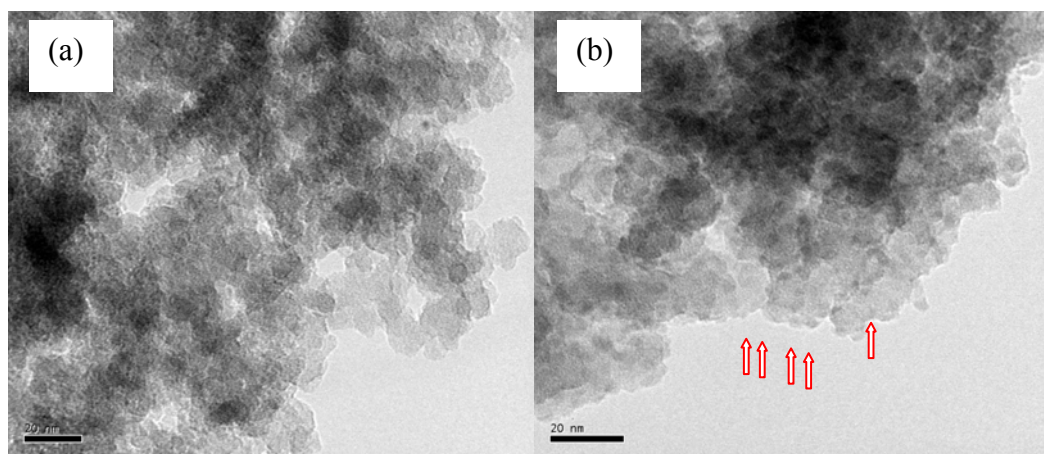


Figure 2: TEM images of TiO₂/SiO₂ containing (a) 12 wt% TiO₂ and (b) 40 wt% TiO₂, where the red arrows point towards the TiO₂(A) crystallites

The electronic structures of this series of supported $\text{TiO}_2/\text{SiO}_2$ samples were examined with *in situ* UV-Vis spectroscopy, a characterization technique that provides information about the local electron density of the supported titania phase. The edge energy, or E_g value, for the different supported titania samples increases continuously as the TiO_x domain size becomes smaller (see Figure 3). Larger band gap values correspond to higher local electron density and less electron delocalization, which correspond to less reducible metal oxides. This trend reflects the well-known quantum confinement effect for small dimensions.

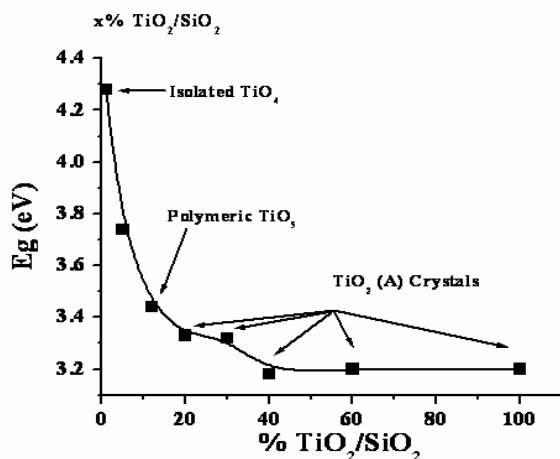


Figure 3: UV-vis edge energy, E_g , dependence on TiO_2 loading of supported $\text{TiO}_2/\text{SiO}_2$

Supported 5% $\text{WO}_3/\text{TiO}_2/\text{SiO}_2$. Raman spectroscopy demonstrated that crystalline WO_3 particles were not present and that all the tungsten oxide self-assembled on titania as surface WO_x species. The dehydrated surface WO_x species were always associated with the titania component since surface WO_x on SiO_2 gives rise to a Raman band at $\sim 980 \text{ cm}^{-1}$ and the dehydrated surface WO_x species on TiO_2 give rise to a Raman band at $\sim 1014 \text{ cm}^{-1}$ [20]. The $\sim 1014 \text{ cm}^{-1}$ Raman band has previously been associated with highly distorted surface WO_6 species [21]. The surface WO_x species maintained the same molecular structure as a function of the TiO_2 content as reflected in the constant terminal $\text{W}=\text{O}$ Raman vibration at $\sim 1014 \text{ cm}^{-1}$. The electronic structure of the surface WO_x species could not be accurately determined for this catalyst system because of the strong UV-Vis absorption by the TiO_2 component of the supported $\text{WO}_3/\text{TiO}_2/\text{SiO}_2$ catalyst system in the region of interest.

The surface chemistry of the highly distorted surface WO_6 species was chemically probed with CH_3OH -temperature programmed surface reaction (TPSR) spectroscopy. The surface WO_6 species possess acidic characteristics by exclusively yielding DME as the reaction product. The DME T_p temperature was found to systematically increase with increasing TiO_2 domain size (Table 1 and Figure 4). Increasing T_p values reflects decreasing catalytic activity of the active surface WO_6 sites. This reveals that the intrinsic catalytic activity of acidic surface WO_6 sites can be varied by tuning the electron density of the of the underlying TiO_2 nano-ligand. Thus, small titania domains decrease the extent of electron delocalization and enhance the catalytic activity of non-reducible catalytic acid sites. The corresponding selectivity also depends on the relative rate constants of the individual reaction steps. The CH_3OH -TPSR results were confirmed in corresponding steady-state CH_3OH dehydration catalytic reaction studies.

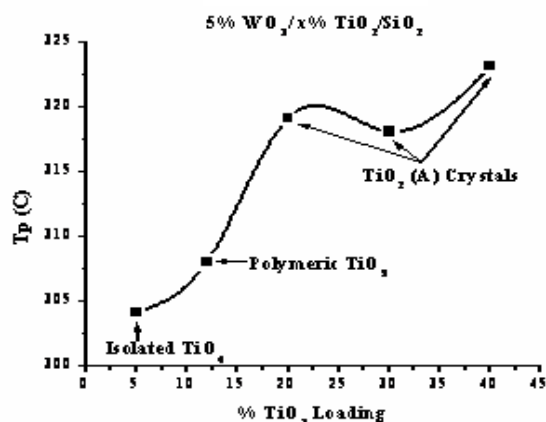


Figure 4: CH₃OH-TPSR Tp values versus TiO₂ loading for 5% WO₃/TiO₂/SiO₂.

Supported 5% V₂O₅/TiO₂/SiO₂. Raman spectroscopy demonstrated that crystalline V₂O₅ particles were not formed and that all the vanadia self-assembled as surface VO_x species on the titania. The surface vanadia species maintained a constant molecular structure as a function of TiO₂ content as reflected in the constant V=O Raman vibration at ~1031 cm⁻¹, which is known from previous solid state ⁵¹V NMR [22, 23], XANES/EXAFS [24], and UV-Vis DRS [25] studies to possess VO₄ coordination and one terminal V=O bond and three bridging V-O- bonds [26]. The electronic structure of the surface VO_x species could not be accurately determined for this catalyst system because of the strong UV-Vis absorption by the TiO₂ component of the supported V₂O₅/TiO₂/SiO₂ catalyst system in the region of interest.

The surface chemistry of the surface VO₄ vanadia species on the TiO₂ (anatase)/SiO₂ support were chemically probed with CH₃OH-temperature programmed surface reaction (TPSR) spectroscopy. The surface VO₄ species possess redox characteristics by exclusively yielding H₂CO as the reaction product. The H₂CO Tp temperature was found to systematically decrease with increasing TiO₂ domain size (Table 1 and Figure 5). Decreasing Tp temperatures reflects increasing catalytic activity of the active surface VO₄ sites. This shows that the intrinsic catalytic activity of redox surface VO₄ sites can be varied by controlling the electron density of the of the underlying TiO₂ nano-ligand. Thus, small TiO₂ domains increase the extent of electron delocalization and enhance the catalytic activity of non-reducible catalytic redox sites.

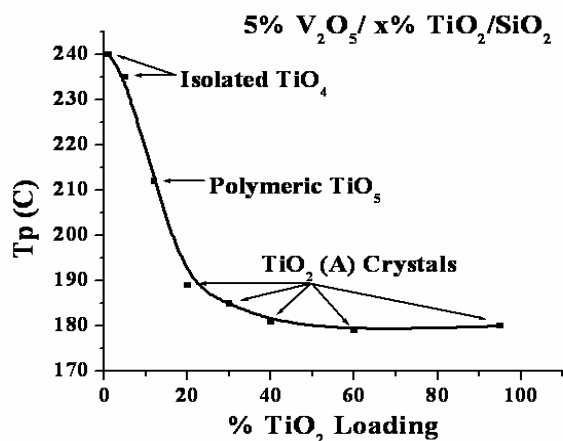


Figure 5: CH₃OH-TPSR Tp values versus % TiO₂ loading for 5% V₂O₅/TiO₂/SiO₂

Significance

These experimental results demonstrate *for the first time* that varying the local electron density of oxide nanoligand supports allows tuning of the catalytic activity as well as selectivity of acidic surface metal oxide catalytic active sites. Additional steady state catalytic reaction studies with different reactions are needed to determine the effect of this electronic tuning by oxide nanoligands on the resulting reaction selectivity.

This investigation also demonstrates how to molecularly engineer well-defined nano-oxide domains and fully determine their electronic and molecular structures with multiple *in situ* molecular spectroscopic methods (UV-Vis, Raman, XANES/EXAFS, solid state NMR and TEM). Combining this fundamental electronic and molecular structural information with corresponding catalytic activity and selectivity measurements allows for the establishment of electronic/molecular structure-catalytic activity/selectivity relationships. These new insights will assist in the design of novel supported metal oxide catalysts for different reactions where the oxide support ligand domain size is a critical factor upon the resulting physical and chemical properties of supported catalytic active sites.

References

1. C. T. Thomas, *Catalytic Processes and Proven Catalysts*. New York: Academic Press, 1970.
2. K. Weissmehl and H.-J. Arpe, *Industrial Organic Chemistry*. Weinheim: Verlag Chemie, 1978.
3. R. J. Farrauto and C. H. Bartholomew, *Fundamentals of Industrial Catalytic Processes*. London: Chapman & Hall, 1997.
4. M. Boudart and Mariadosu-Djega, *Kinetics of Heterogeneous Catalysis*. Princeton: Princeton University Press, 1984.
5. G. C. Bond and D. T. Thompson, *Catal. Rev.-Sci. Eng.* **41** (1999) 319-388.
6. Q. Fu, H. Saltsburg, and M. Flytzani-Stephanopoulos, *Science* **301** (2003) 935-938.
7. R. J. Davis, *Science* **301** (2003) 926-927.
8. M. Jacoby. *Chem. & Eng. News*, Aug. 30 2004.
9. G. Deo and I. E. Wachs, *J. Catal.* **129** (1991) 307-312.
10. A. Khodakov, B. Olthof, A. T. Bell, and E. Iglesia, *J. Catal.* **181** (1999) 205-216.
11. J. Macht, C. D. Baertsch, M. May-Lozano, S. L. Soled, Y. Wong, and E. Iglesia, *J. Catal.* **227** (2004) 479-491.
12. R. S. Weber, *J. Catal.* **151** (1995) 470-474.
13. M. Fernandez-Garcia, A. Martinez-Arias, J. C. Hanson, and J. A. Rodriguez, *Chem. Rev.* **104** (2004) 4063-4104.
14. X. Gao, S.R. Bare, J.L.G. Fierro, M.A. Banares and I.E. Wachs, *J. Phys. Chem. B* **87** (1998) 5653.
15. W.N. Delgass, G.L. Haller, R. Kellerman and J.H Lunsford, *Spectroscopy in Heterogeneous Catalysts*. Academic Press: New York, 1979.
16. T. Feng and J.M. Vohs, *J. Catal.* **208** (2002) 301.
17. L.E. Briand, W.E. Farneth and I.E. Wachs, *Catal. Today* **219** (2000)
18. J. M. Tatibouët, *Appl. Catal. A-Gen.* **148** (1997) 213-252.
19. M. Badlani and I. E. Wachs, *J. of Catal.* **75** (2001) 137-149.

20. D. S. Kim, M. Ostromecki, and I. E. Wachs, *J. Mol. Catal. A-Chem.* **106** (1996) 93-102 .
21. F. Hilberg, H. E. Gobel, H. Knözinger, H. Schmelz, and B. Lengeler, *J. Phys. Chem.* **95** (1991) 6973-6978.
22. H. Eckert and I. E. Wachs, *J. Phys. Chem.* **93** (1989) 6796-6805.
23. N. Das, H. Eckert, H. Hu, I. E. Wachs, J. F. Walzer, and F. J. Feher, *J. Phys. Chem.* **97** (1993) 8240-8243.
24. T. Tanaka, H. Yamashita, R. Tsuchitani, T. Funabiki, and S. Yoshida, *J. Chem. Soc., Faraday Trans.* **84** (1988) 2987-2999.
25. X. Gao and I. E. Wachs, *J. Catal.* **104** (2000) 1261-1268.
26. G. Rami, C. Christiani, P. Forzatti, and G. Busca, *J. Catal.*, (1990) 574-576.